



Nuclear Instruments and Methods in Physics Research A

journal homepage: www.elsevier.com/locate/nima

Response of the CALICE Si-W electromagnetic calorimeter physics prototype to electrons

C. Adloff^a, Y. Karyotakis^a, J. Repond^b, J. Yu^c, G. Eigen^d, C.M. Hawkes^e, Y. Mikami^e, O. Miller^e, N.K. Watson^e, J.A. Wilson^e, T. Goto^f, G. Mavromanolakis^f, M.A. Thomson^f, D.R. Ward^f, W. Yan^f, D. Benchechrone^g, A. Hoummada^g, M. Krim^g, M. Benyamna^h, D. Boumediene^h, N. Brun^h, C. Cârloganu^{h,*}, P. Gay^h, F. Morisseau^h, G.C. Blazeyⁱ, D. Chakrabortyⁱ, A. Dyshkantⁱ, K. Francisⁱ, D. Hedinⁱ, G. Limaⁱ, V. Zutshiⁱ, J.-Y. Hostachy^j, L. Morin^j, N. D'Ascenzo^k, U. Cornett^k, D. David^k, R. Fabbri^k, G. Falley^k, K. Gadow^k, E. Garutti^k, P. Göttlicher^k, T. Jung^k, S. Karstensen^k, V. Korbel^k, A.-I. Lucaci-Timoce^k, B. Lutz^k, N. Meyer^k, V. Morgunov^k, M. Reinecke^k, F. Sefkow^k, P. Smirnov^k, A. Vargas-Trevino^k, N. Wattimena^k, O. Wendt^k, N. Feege^l, M. Groll^l, J. Haller^l, R.-D. Heuer^l, S. Richter^l, J. Samson^l, A. Kaplan^m, H.-Ch. Schultz-Coulon^m, W. Shen^m, A. Tadday^m, B. Bilkiⁿ, E. Norbeckⁿ, Y. Onelⁿ, E.J. Kim^o, N.I. Baek^p, D.-W. Kim^p, K. Lee^p, S.C. Lee^p, K. Kawagoe^q, Y. Tamura^q, D.A. Bowerman^r, P.D. Dauncey^r, A.-M. Magnan^r, H. Yilmaz^r, O. Zorba^r, V. Bartsch^s, M. Postranecky^s, M. Warren^s, M. Wing^s, M. Fauci Giannelli^t, M.G. Green^t, F. Salvatore^t, M. Bedjidian^{u,v,w}, R. Kieffer^{u,v,w}, I. Laktineh^{u,v,w}, D.S. Bailey^x, R.J. Barlow^x, M. Kelly^x, R.J. Thompson^x, M. Danilov^y, E. Tarkovsky^y, N. Baranova^z, D. Karmanov^z, M. Korolev^z, M. Merkin^z, A. Voronin^z, A. Frey^{aa,1}, S. Lu^{aa}, K. Prothmann^{aa}, F. Simon^{aa}, B. Bouquet^{ab}, S. Callier^{ab}, P. Cornebise^{ab}, J. Fleury^{ab}, H. Li^{ab}, F. Richard^{ab}, Ch. de la Taille^{ab}, R. Poeschl^{ab}, L. Raux^{ab}, M. Ruan^{ab}, N. Seguin-Moreau^{ab}, F. Wicek^{ab}, M. Anduze^{ac}, V. Boudry^{ac}, J.-C. Brient^{ac}, G. Gaycken^{ac}, P. Mora e Freitas^{ac}, G. Musat^{ac}, M. Reinhard^{ac}, A. Rougé^{ac}, J.-Ch. Vanel^{ac}, H. Videau^{ac}, K.-H. Park^{ad}, J. Zacek^{ae}, J. Cvach^{af}, P. Gallus^{af}, M. Havranek^{af}, M. Janata^{af}, M. Marcisovsky^{af}, I. Polak^{af}, J. Popule^{af}, L. Tomasek^{af}, M. Tomasek^{af}, P. Ruzicka^{af}, P. Sicho^{af}, J. Smolik^{af}, V. Vrba^{af}, J. Zalesak^{af}, B. Belhorma^{ag}, M. Belmir^{ag}, S.W. Nam^{ah}, I.H. Park^{ah}, J. Yang^{ah}, J.-S. Chai^{ai}, J.-T. Kim^{ai}, G.-B. Kim^{aj}, J. Kang^{aj}, Y.-J. Kwon^{aj}

^a Laboratoire d'Annecy-le-vieux de Physique des Particules, Chemin du Bellevue BP 110, F-74941 Annecy-le-Vieux Cedex, France^b Argonne National Laboratory, 9700 S. Cass Avenue, Argonne, IL 60439-4815, USA^c University of Texas, Arlington, TX 76019, USA^d University of Bergen, Institute of Physics, Allegaten 55, N-5007 Bergen, Norway^e University of Birmingham, School of Physics and Astronomy, Edgbaston, Birmingham B15 2TT, UK^f University of Cambridge, Cavendish Laboratory, J.J. Thomson Avenue, CB3 0HE, UK^g Université Hassan II An Chock, Faculté des sciences. B.P. 5366 Maarif, Casablanca, Morocco^h Laboratoire de Physique Corpusculaire de Clermont-Ferrand (LPC), 24 avenue des Landais, 63177 Aubière Cedex, Franceⁱ NICADD, Northern Illinois University, Department of Physics, DeKalb, IL 60115, USA^j Laboratoire de Physique Subatomique et de Cosmologie - Université Joseph Fourier Grenoble 1 - CNRS/IN2P3 - Institut Polytechnique de Grenoble, 53, rue des Martyrs, 38026 Grenoble Cedex, France^k DESY, Notkestrasse 85, D-22603 Hamburg, Germany^l University of Hamburg, Physics Department, Institut für Experimentalphysik, Luruper Chaussee 149, 22761 Hamburg, Germany^m University of Heidelberg, Fakultät für Physik und Astronomie, Albert Überle Str. 3-5 2.OG Ost, D-69120 Heidelberg, Germanyⁿ University of Iowa, Department of Physics and Astronomy, 203 Van Allen Hall, Iowa City, IA 52242-1479, USA^o Chonbuk National University, Jeonju 561-756, South Korea^p Kangnung National University, HEP/PD, Kangnung, South Korea^q Department of Physics, Kobe University, Kobe 657-8501, Japan^r Imperial College, Blackett Laboratory, Department of Physics, Prince Consort Road, London SW7 2BW, UK^s Department of Physics and Astronomy, University College London, Gower Street, London WC1E 6BT, UK^t Royal Holloway University of London, Department of Physics, Egham, Surrey TW20 0EX, UK^u Université de Lyon, F-69622, Lyon, France^v Université de Lyon 1, Villeurbanne, France^w CNRS/IN2P3, Institut de Physique Nucléaire de Lyon, France^x The University of Manchester, School of Physics and Astronomy, Schuster Lab, Manchester M13 9PL, UK^y Institute of Theoretical and Experimental Physics, B. Cheremushkinskaya ul. 25, RU-117218 Moscow, Russia^z M.V. Lomonosov Moscow State University, D.V. Skobeltsyn Institute of Nuclear Physics (SINP MSU), 1/2 Leninskiye Gory, Moscow 119991, Russia

^a Max Planck Inst. für Physik, Föhringer Ring 6, D-80805 Munich, Germany^{ab} Laboratoire de L'accélérateur Linéaire, Centre d'Orsay, Université de Paris-Sud XI, BP 34, Bâtiment 200, F-91898 Orsay Cedex, France^{ac} École Polytechnique, Laboratoire Leprince-Ringuet (LLR), Route de Saclay, F-91128 Palaiseau Cedex, France^{ad} Pohang Accelerator Laboratory, Pohang 790-784, South Korea^{ae} Charles University, Institute of Particle and Nuclear Physics, V Holesovickach 2, CZ-18000 Prague 8, Czech Republic^{af} Institute of Physics, Academy of Sciences of the Czech Republic, Na Slovance 2, CZ-18221 Prague 8, Czech Republic^{ag} Centre National de l'Energie, des Sciences et des Techniques Nucléaires, B.P. 1382, R.P. 10001, Rabat, Morocco^{ah} Ewha Womans University, Department of Physics, Seoul 120, South Korea^{ai} Sungkyunkwan University, 300 Cheoncheon-dong, Jangan-gu, Suwon, Gyeonggi-do 440-746, South Korea^{aj} Yonsei University, Department of Physics, 134 Sinchon-dong, Sudaemoon-gu, Seoul 120-749, South Korea

ARTICLE INFO

Article history:

Received 21 November 2008

Received in revised form

18 July 2009

Accepted 20 July 2009

Available online 28 July 2009

Keywords:

CALICE

ILC

Electromagnetic calorimeter

Silicon detector

Electron reconstruction

ABSTRACT

A prototype silicon–tungsten electromagnetic calorimeter (ECAL) for an international linear collider (ILC) detector was installed and tested during summer and autumn 2006 at CERN. The detector had 6480 silicon pads of dimension $1 \times 1 \text{ cm}^2$. Data were collected with electron beams in the energy range 6–45 GeV. The analysis described in this paper focuses on electromagnetic shower reconstruction and characterises the ECAL response to electrons in terms of energy resolution and linearity. The detector is linear to within approximately the 1% level and has a relative energy resolution of $(16.53 \pm 0.14(\text{stat}) \pm 0.4(\text{syst})) / \sqrt{E(\text{GeV})} \oplus (1.07 \pm 0.07(\text{stat}) \pm 0.1(\text{syst})) (\%)$. The spatial uniformity and the time stability of the ECAL are also addressed.

© 2009 Elsevier B.V. All rights reserved.

1. Introduction

The CALICE Collaboration is conducting R&D into calorimetric systems for the ILC [1]—a proposed e^+e^- linear collider intended to operate at a centre of mass energy ranging up to the TeV scale. The physics scope at the ILC includes precise measurements of the triple- and quartic-gauge bosons interactions, as well as the complete characterisation of the Higgs-boson and top-quark sectors. In addition, searches for physics beyond the Standard Model could most often be addressed in a model-independent way.

The final states are typically multiple hadronic jets, accompanied frequently by low-momentum leptons and/or missing energy. The signature of the final states of interest often relies on the identification of Z or/and W bosons in their decay modes into two jets. In order to distinguish them efficiently, a jet energy resolution close to $30\%/\sqrt{E/\text{GeV}}$ has to be achieved [1]. A precise reconstruction of the jet direction (few mrad/ $\sqrt{E/\text{GeV}}$) is also required. These are among the main requirements driving the detector design in general at the ILC and the calorimetry design in particular.

The target jet energy resolution represents an improvement by a factor close to two over the best obtained in previous detectors. Moreover the detection environment becomes more complex with increasing centre-of-mass energy. A promising way to achieve this increase in resolution is through designing a detector system optimised for the so called “particle flow” approach [2], which relies on the separate reconstruction of as many particles in the jet as possible, using the most suitable detector systems.

The success of such an algorithm depends on the quality of the pattern recognition in the calorimeters. For particle flow, a high spatial granularity is therefore as important as the intrinsic energy resolution for single particles. Furthermore, the overall design of the detector (tracking, electromagnetic and hadronic calorimetry) needs to be considered in a coherent way.

The design of the ILC detectors can be optimised using Monte Carlo simulations, but in order to do this, it is crucial to validate the Monte Carlo tools with data. Therefore, the R&D of the CALICE Collaboration has two broad aims. The first is to construct realistic calorimeter prototypes, and learn about their operation and behaviour in beam-tests. The second objective is to compare the data with Monte Carlo simulations using the same tools as those used for the full detector. This is especially important in the case of hadronic showers, for which many models are available, with differing predictions for the calorimeter response. The CALICE plan is to expose complete calorimeter systems (electromagnetic and hadronic, using various technologies) to test beams of electrons, muons and hadrons. To this end, a first round of beam-tests was performed at DESY and CERN in summer 2006, using a silicon–tungsten sampling electromagnetic calorimeter [3], followed by a hadron calorimeter composed of iron and scintillator tiles [4], and then a tail catcher and muon counter (TCMT) of iron instrumented with scintillator strips [5].

In this paper, the results of exposure of the prototype to electron beams in the energy range 6–45 GeV at the CERN H6 beam line [6] are reported. The layout of the beam-tests is outlined in Section 2. The ECAL is briefly described in Section 3 and some key technical aspects of its performance are highlighted. Section 4 summarises the Monte Carlo simulation. Features of the electron beam data are reviewed in Section 5 and the uniformity across the detector is addressed. The results of the energy measurements together with some of their systematic uncertainties are presented in Section 6 for the detector areas of uniform response.

Several other studies of the prototype are ongoing, exploiting its unprecedentedly fine segmentation and capacity to observe shower development in detail. These studies will be reported in subsequent publications.

2. Experimental setup

A sketch of the CERN H6 [6] test-beam setup is presented in Fig. 1 and a detailed description of the detectors can be found in Ref. [3]. The beam trigger was defined by the coincidence signal of two of the three scintillator counters (referred to as Sc2, Sc3 and

* Corresponding author.

E-mail address: carlogan@in2p3.fr (C. Carloganu).

¹ Now at Universität Göttingen.

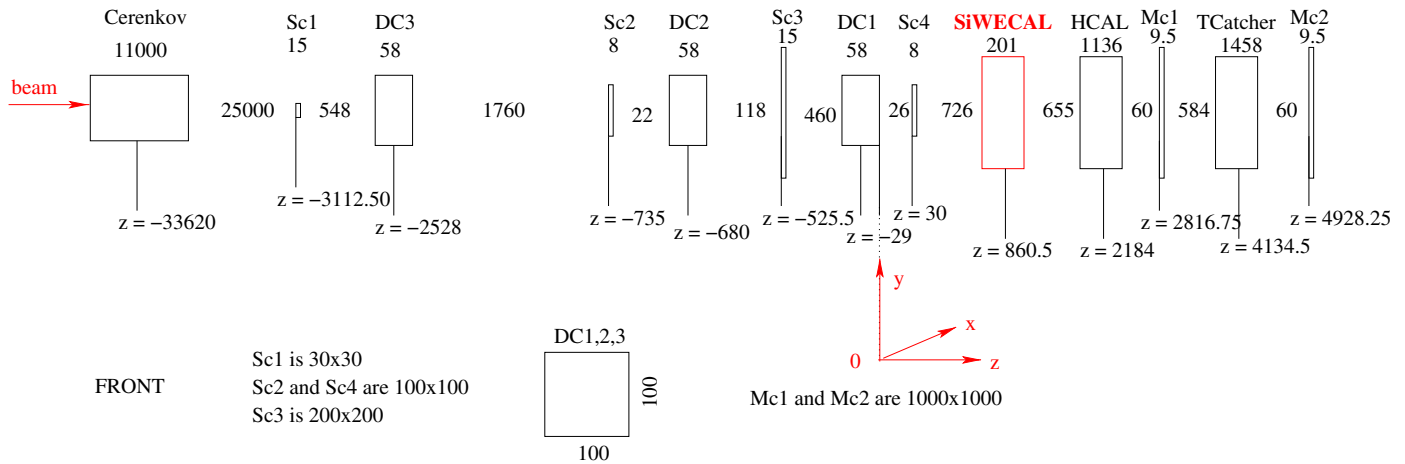


Fig. 1. Sketch of the CERN test-beam setup. The right-handed coordinate system used hereafter is indicated. All distances and dimensions are in mm.

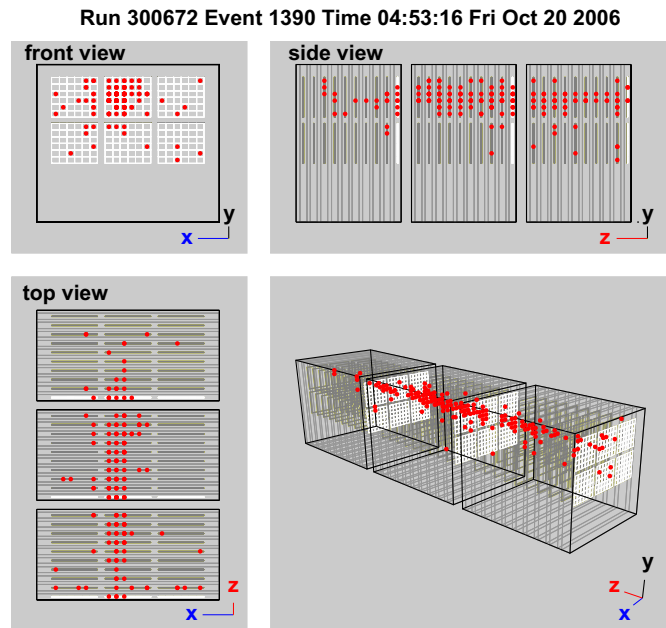


Fig. 2. A typical 10 GeV electron shower in the ECAL, as seen in the online event display. Only detector cells having energies higher than 0.5 MIPs are displayed. Layout not to scale.

Sc4 in Fig. 1) present in the beam. When it was not used in the trigger, the largest scintillator (Sc3) was still read out and so could be used as a beam halo veto offline. In addition, three drift chambers (DC1, DC2, DC3) were available for monitoring the beam and reconstructing the tracks. The tracking information is not however used for the present study, which relies exclusively on the ECAL for reconstructing both the position and the energy of the electrons. A threshold Cherenkov detector was used for e/π discrimination. The coordinate system used is right-handed. The surface of the drift chamber (DC1) closest to the ECAL defines the origin, the z axis is the beam axis and x and y are the horizontal and upward-vertical axes, respectively.

The physics program and the overall electron, pion and muon statistics collected are extensively discussed in Ref. [3]. This paper presents the measurement of the ECAL response to electrons normally incident on the calorimeter surface. The event display for one of these events is shown in Fig. 2, where the energy of the hits is measured in MIP units, one MIP being the signal left by a minimum ionising particle.

3. The Si-W ECAL prototype

A detailed description of the ECAL hardware is given in Ref. [3], along with details of the commissioning and a number of technical features of the calibration and performance of the system. The ECAL prototype consisted of 30 layers of tungsten, the first 10 of thickness 1.4 mm, the next 10 of 2.8 mm and the last 10 of 4.2 mm, comprising 24 radiation lengths in total at normal incidence. The development of the showers was sampled using 30 layers of silicon PIN diode pads interleaved between the tungsten plates. The silicon thickness was 525 μm , with each pad having a transverse area of $1 \times 1 \text{ cm}^2$. The sensors were implemented on 4 in.² wafers, segmented into 6×6 pads. At the time of the 2006 CERN beam-tests, each layer consisted of a 3×2 array of wafers, i.e. 18 pads horizontally and 12 pads vertically, leading to a total of 6480 pads for the ECAL.

A particular effort has been made to minimise passive material zones and to keep the calorimeter as compact as possible, by incorporating half of the tungsten into alveolar composite structures. Three independent structures can be distinguished, as shown in Fig. 3, left, one for each thickness of tungsten. Each structure is fabricated by moulding preimpregnated carbon fibre and epoxy onto tungsten sheets, leaving free spaces between two layers to insert the detection units, called detector slabs. The slab is shielded on both sides from the tungsten alveolar structure by an aluminium foil 0.1 mm thick, to protect the silicon modules from electromagnetic noise and provide the wafer substrate ground.

The passive area between wafers is mainly due to two 1 mm wide guard rings around them, called in the following “inter-wafer gaps”. To reduce their overlapping, the two detection layers of each slab are offset by 2.5 mm in the x direction, as it can be seen in Fig. 3, right, where two successive slabs are shown. Furthermore, the slabs in each substructure are offset by 1.3 mm in the x direction. The expected accuracy for the positioning of each module is $\pm 0.05 \text{ mm}$.

Blocks of random triggers were recorded during data-taking in order to monitor pedestals and noise. Short-term changes and shifts in pedestals caused by large signals in neighbouring cells were monitored and corrected using cells without signal in beam events [3]. The uncertainty on the pedestal levels was estimated to be less than 0.002 MIPs, negligible compared to the energy deposited by electron showers (a 10 GeV electron deposits on average 1450 MIPs). The noise level was typically 0.13 MIPs; its spread channel-to-channel was 9% of the mean noise and the spread run-to-run was less than 1% of the mean noise. The low

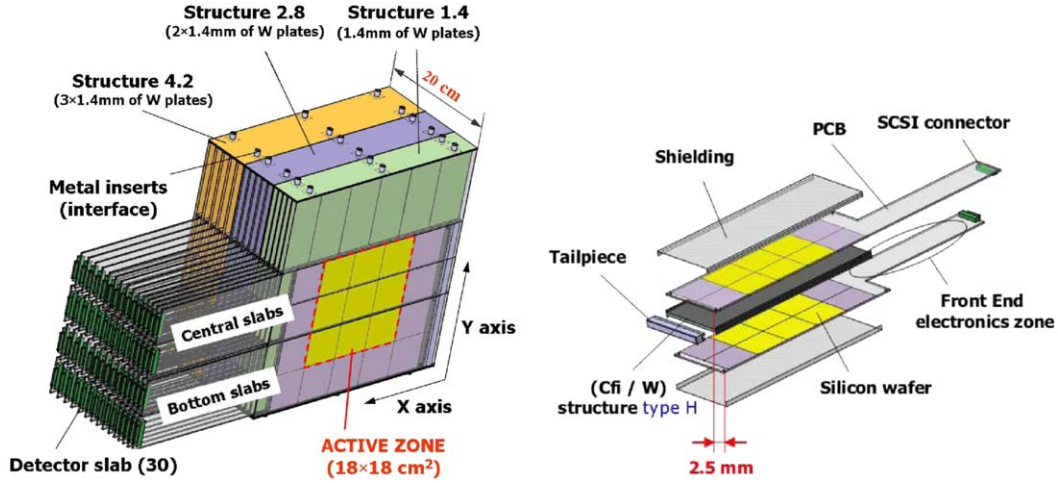


Fig. 3. Schematic view of the ECAL (left) and a zoom showing the components and the geometry of a detector slab (right). Only the two central slabs of the prototype were present for the 2006 beam-tests.

spread of the noise justifies the use of a single energy threshold for all cells in the detector for this study.

Calibration constants for each pad were determined using muon events. The response of each cell was fitted by a convolution of a Landau distribution with a Gaussian. The most probable value of the underlying Landau function was taken to define the MIP value for each cell, and the raw energy for each cell in data was corrected to units of MIPs. All but 9 pads were functioning and successfully calibrated. The calibration constants were determined with an accuracy of 0.5% and had a cell-to-cell dispersion of 5%. Data taken in the various beam-test periods during summer and autumn 2006 showed well correlated calibration constants, with a systematic shift less than 1.6% of a MIP.

One feature of the data which has not been accounted for in the detector simulation is associated with showers which deposit a sizeable energy in the guard ring surrounding a wafer. This is a cause of correlated cross-talk, observed as a distinctive square pattern of low-energy hits in a number of cells around the periphery of the wafer. The prevalence of this effect increases with the shower energy crossing the guard ring and therefore its rate is significantly reduced when considering only electrons impinging on the centre of the wafers. In the future, the design of the guard rings will be modified in order to minimise this problem.

After calibration, the ECAL data consist of hits in the cells of the calorimeter with energies in units of MIPs. Even if all of the hit pads are recorded and kept at the reconstruction level, a threshold cut of 0.6 MIPs was imposed on each cell (almost five times the mean noise level) for this study. Such a cut is highly effective in removing most of the noise signals: only 0.8% of the cells have signals higher than 0.2 MIPs in absence of beam. The cut value is varied in some of the systematic checks described later.

4. Monte Carlo simulation

The test-beam setup is simulated with Mokka [7], a Geant4-based [8] Monte Carlo program, followed by a digitisation module simulating the response of the front-end and readout electronics. The simulation starts 60 m upstream of the ECAL and includes all known material budget along the path of the beam: ~ 0.28 radiation lengths, mainly in the form of air and scintillators. The CERN H6 beam-chambers and the collimators were not simulated. The sub-detectors are simulated with different levels of detail, depending on their impact on the physics analysis: material simulation only for the Cherenkov detectors, raw energy deposi-

tions stored for the trigger counters, partial electronics simulation for the tracking detectors. In the case of the ECAL, the detector sub-modules and slabs are supposed to be perfectly aligned, both in x and y directions. The simulation gives the raw energy depositions in the Si pads and the readout electronics is simulated assuming that each channel exhibits only Gaussian noise. The mean values of the noise for each channel follow a Gaussian distribution over the ECAL, with the mean value of 0.13 and 0.012 MIPs dispersion, as measured. Since 99.9% of the ECAL cells were functioning, the impact of the non-responding cells is expected to be small and their signals were not suppressed in the simulation for this analysis.

The beam divergence was measured using the drift chambers to be ~ 0.5 mrad. The induced displacement over the 200 mm length of the ECAL (0.1 mm) is negligible compared to the width of the sensor and of the inter-wafer gaps. The beam simulation assumes therefore a parallel beam with Gaussian width reproducing the observed beam profile, as measured using the distribution of the shower centroids. To study systematic effects due to lateral leakage of the showers, samples are also generated with a beam spread uniformly over the ECAL front-face.

A Gaussian momentum dispersion consistent with the settings of the beam collimators [6] is applied for each run. The expected values for this dispersion are given in Table 3.

5. Selection of electron events

Single electron showers are selected using the energy recorded in the ECAL. This energy, E_{raw} , is calculated with the three ECAL modules weighted in proportion to the tungsten thickness

$$E_{\text{raw}} = \sum_{i=0}^{i=9} E_i + 2 \sum_{i=10}^{i=19} E_i + 3 \sum_{i=20}^{i=29} E_i \quad (1)$$

where E_i is the energy deposit in layer i . The distribution of E_{raw} is shown in Fig. 4 for a typical 15 GeV event sample. The electron peak at around 3900 MIPs is clearly visible; however, the muon and pion contamination in the beam gives an additional peak at 85 MIPs and the region between the two main peaks is populated with pions. Electron candidates are selected by requiring

$$125 < \frac{E_{\text{raw}}(\text{MIP})}{E_{\text{beam}}(\text{GeV})} < 375 \quad (2)$$

with the upper limit ensuring the rejection of multiple events. The significant pion contamination present in some of the data runs is

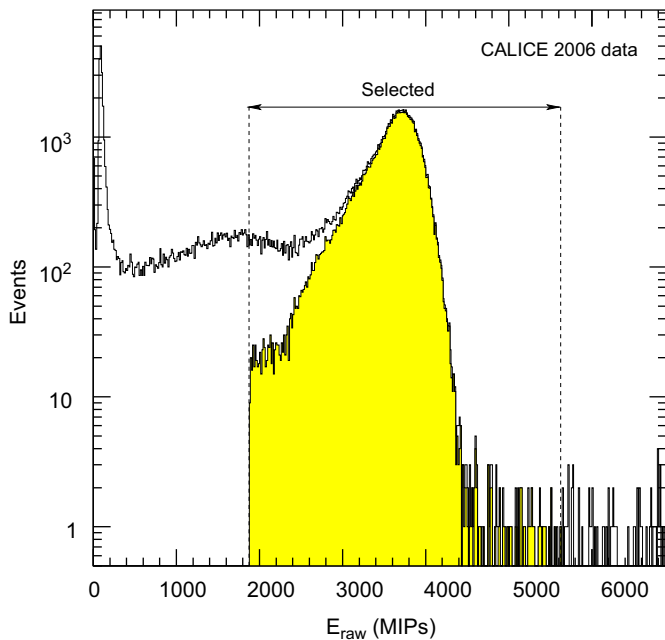


Fig. 4. Distribution of total ECAL hit energies for a 15 GeV electron run with a significant pion content. The E_{raw} selection window and the shaded area obtained by demanding a signal from the Cherenkov counter are shown.

reduced by demanding a trigger signal from the threshold Cherenkov counter in the beam. The effect of this additional requirement is indicated by the shaded region in Fig. 4.

5.1. Selection of showers well contained in the ECAL

The fiducial volume in which the showers are fully contained in the ECAL was estimated using electrons away from the inter-wafer gaps and hitting the central part of the ECAL. The radial shape of an average 45 GeV electron shower is shown in Fig. 5, both for data and simulation. The simulation reproduces the shower width to better than 2%: 95% of the shower energy is contained within 30.5 mm (i.e. less than four pads), to be compared with 29.9 mm in the case of the simulated showers. To ensure radial containment, all electrons impinging on the ECAL front face less than 32 mm from one of the ECAL borders are therefore excluded from the selected sample.

The longitudinal containment of the showers is ensured by rejecting events which have the maximum of the energy deposited along the z direction in the first five layers or the last five layers of the prototype. Only 0.21% of the simulated 6 GeV electrons fail these containment criteria and 0.02% of the 45 GeV electrons.

5.2. Rejection of the beam halo

The beam shape in x and y is measured using the drift chambers and the shower barycentre. Since no ECAL-independent measurement of the beam momentum is available for the 2006 beam-test, the distribution of the beam momentum as a function of x and y is monitored using the ECAL energy-profile versus x and y . The observed distributions show a stable regime, with a width depending on the settings of each run, and a sharp drop towards the edges. The measurement of the shower radial-development (see Section 5.1) and the simulations indicate that this drop is not likely to be due to leakage, but rather to a low-energy halo of the beam. This beam halo is rejected by defining, for each individual run, a x and y acceptance for the incoming electron track such as

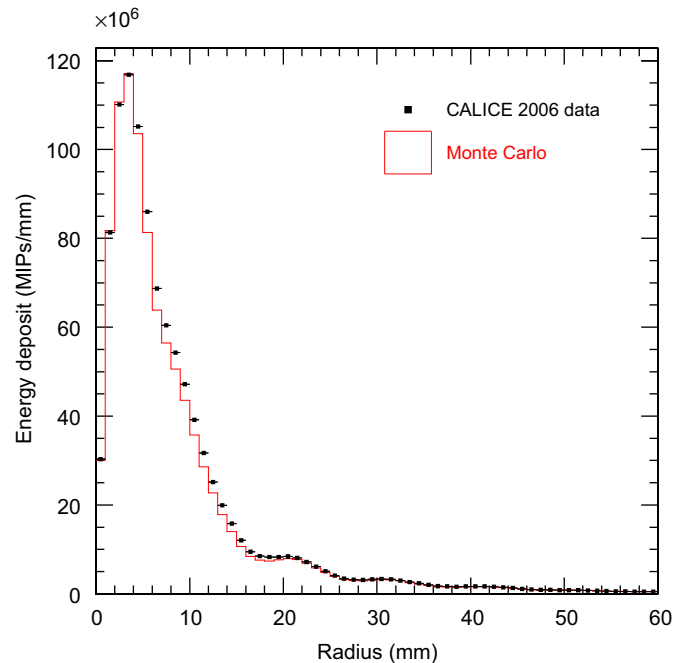


Fig. 5. Energy deposited in ECAL as a function of the radial distance to the longitudinal shower axis, integrated over 171 671 showers of 45 GeV. The artificial peaks around 20 and 30 mm are due to the 1 cm granularity for the y coordinate of the hits.

to achieve a reasonably flat distribution of the mean energy deposition in the ECAL.

5.3. Rejection of electrons showering in front of ECAL

The data recorded at CERN contain a significant number of events which have approximately the expected energy for a single electron, but with a spatial structure clearly distinctive of multiple showers. A likely explanation is bremsstrahlung far upstream in the beam line. In the absence of a complete quantitative description of the material further upstream in the beam line, it is necessary to reject as much as possible multiple electron showers before comparing data and simulation. To this end, the energy deposits in the shower are projected in a two-dimensional histogram, on the transverse, $x-y$, plane. The binning of the histogram is the same in x and y and corresponds to the cell size (1 cm). A simple nearest-neighbour clustering algorithm (including diagonal neighbours) is applied on the bins with energies above a given threshold T , in order to select events with more than one local maximum for the energy deposit. For each event the maximum value of the threshold is determined, T_{max} , above which the event would be reconstructed as a single cluster. The distributions of T_{max} are compared between data and simulation for a 30 GeV beam in Fig. 6. A sizeable discrepancy is seen for larger values of T_{max} and therefore a cut is applied on T_{max} . The cut is energy dependent, varying from 50 MIPs at 10 GeV to 120 MIPs at 45 GeV. This cut typically rejects $\sim 20\%$ of data and $\sim 2-3\%$ of simulated events at the higher energies.

As stated in the beginning of Section 5 and Eq. (1), the energy is reconstructed by summing over all hit pads in the calorimeter, without prior application of a clusterisation algorithm. It is therefore likely that the energy resolution and linearity are not much affected by the radiative losses of the electrons upstream of the ECAL, even if they modify spatially the energy distribution in the ECAL. The effect of the cut on T_{max} will be considered among the systematic uncertainties affecting the results presented here.

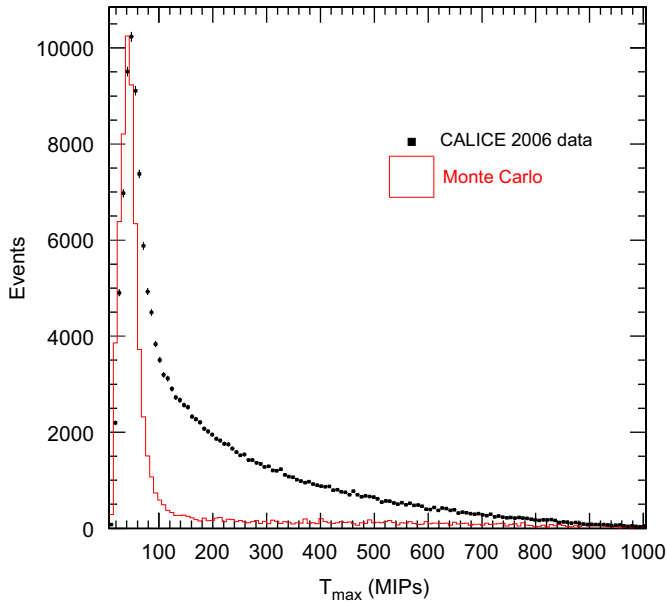


Fig. 6. Distribution of the variable T_{\max} (described in the text), which is used to reduce the contribution of double showers. Data and simulation are compared at 30 GeV.

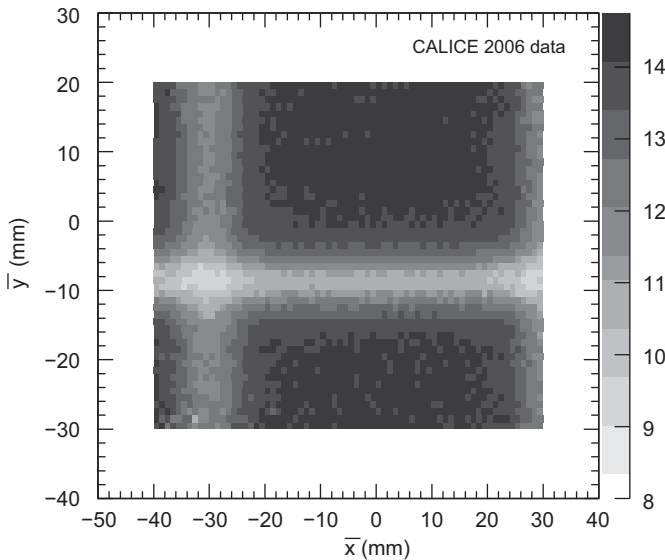


Fig. 7. Mean values of E_{raw} for 15 GeV electrons as a function of the shower barycentre, transverse to the beam direction. The energies have been scaled down by a factor 266 to provide approximate conversion to GeV.

5.4. Inter-wafer gap effect

The “inter-wafer gaps”, the non-active gaps between adjacent Si pads situated on different wafers (2 mm), are significant compared to the transverse shower size and degrade the prototype response when showers traverse them. This is illustrated in Fig. 7 for 30 GeV electrons impinging on the calorimeter at normal incidence. Here the mean value of E_{raw} (Eq. (1)) is plotted as a function of the shower barycentre (\bar{x}, \bar{y}) , defined as

$$(\bar{x}, \bar{y}) = \left(\sum_i (E_i x_i, E_i y_i) / \sum_i E_i \right) \quad (3)$$

The sums run over all hit cells in the calorimeter. Dips in response corresponding to the positions of the guard rings are clearly

visible: the energy loss is about 15% when electrons impinge in the centre of the x gaps and about 20% in the case of the y gap. The gap in x is shallower and wider than that in y , due to the staggering of the gaps in x (see Section 3 and Ref. [3]). In order to recover this loss and to have a more uniform response of the calorimeter, a simple method was investigated. The ECAL energy response, $f(\bar{x}, \bar{y}) = E_{\text{raw}}/E_{\text{beam}}$, is measured using a combined sample of 10, 15 and 20 GeV electrons, equally populated.

The response function f , normalised such as to have a unit response in the middle of the wafers, is displayed in Fig. 8. To characterise the x (y) response, the events were required to be outside the inter-wafer gap in y (x), leading to an important difference in the number of events for the two distributions, since the beam is centred on the y gap. It can be parametrised with Gaussian functions, independently in \bar{x} and \bar{y} :

$$f(\bar{x}, \bar{y}) = \left(1 - a_x \exp \left(-\frac{(\bar{x} - x_{\text{gap}})^2}{2\sigma_x^2} \right) \right) \left(1 - a_y \exp \left(-\frac{(\bar{y} - y_{\text{gap}})^2}{2\sigma_y^2} \right) \right). \quad (4)$$

Here, x_{gap} and y_{gap} are the positions at the centres of the gaps in x and y , respectively, a_x (a_y) and σ_x (σ_y) their respective depths and widths in the two directions. The results of the Gaussian parametrisations are given in Table 1.

The variation of the impact of the inter-wafer gaps with the energy of the electron shower and the expectations from the simulations are shown in Table 2. Generally, the inter-wafer gap effect is more pronounced in the simulations than in the data and two effects may be held responsible for it. Possible misalignments of the different detector sub-modules and slabs are not taken into account in the simulation at the moment. The second effect which tends to reduce the influence of the inter-wafer gaps for the data is the cross-talk issue discussed in Section 3. Part of the energy deposited in the guard ring surrounding a wafer is distributed by cross-talk into the edge pixels of the wafers and therefore recovered as visible energy. Since this effect increases with the energy deposited in the gap, the higher the shower energy is, the higher will be its impact.

As illustrated in Fig. 9, when the energy of each shower is corrected by $1/f$, the average energy loss in the gaps is reduced to a few percent level. The low-energy tail in the energy distribution is also much reduced (Fig. 10, left). The remaining tail is most likely due to the imperfections of the crude corrections applied in this analysis, but is nevertheless reasonably well reproduced by the simulation (Fig. 10, right). The correction method relies only on calorimetric information and can be applied both for photons and electrons.

Even though it is possible to correct for the inter-wafer gaps on average, for individual events their presence will induce fluctuations in the energy response and degrade the ECAL resolution compared to a homogeneous calorimeter. In the data described here, the beam centre was close to the inter-wafer gap in y , artificially increasing the impact of the inter-wafer gaps compared to an experiment with a beam uniformly spread over the ECAL front face. Moreover, since the beam width varies strongly with the beam energy (the RMS is approximately 22 mm in the y direction at 6 GeV, but only 7 mm at most at 45 GeV), the impact of the energy lost in the gaps is different at each energy: 58% (56%) of the selected electrons at 6 GeV are within four standard deviations of the x (y) inter-wafer gaps, to be compared with 40% (68%) at 30 GeV and 20% (66%) at 45 GeV. Therefore, in order to assess the energy response and resolution of the prototype as a function of energy in a unbiased way, only particles impinging in the middle of the wafers are selected. Since the gap effect is negligible more than four standard deviations away from the gap

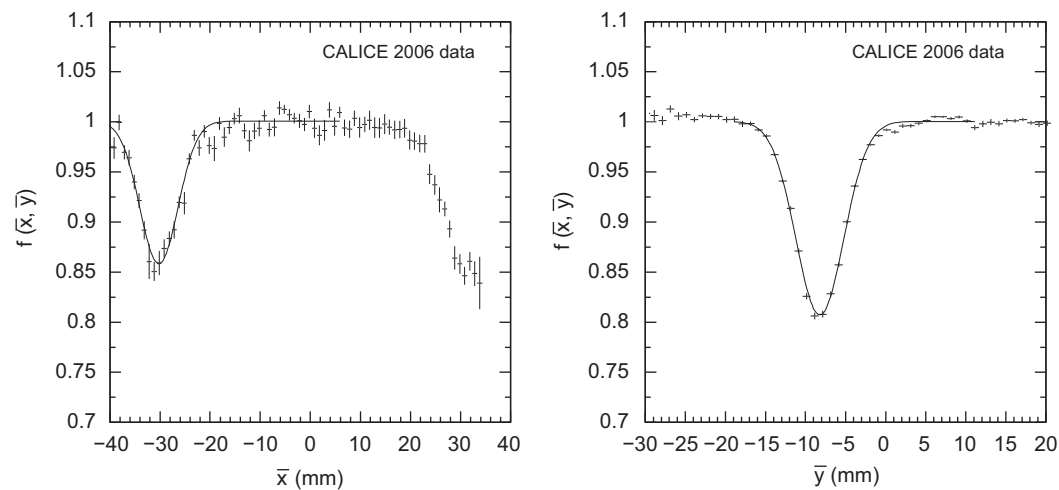


Fig. 8. Normalised $f(\bar{x}, \bar{y})$ as a function of the shower barycentre coordinates, for a combined sample of 10, 15 and 20 GeV electrons. The data points are shown together with the fitted form of $f(x, y)$, as explained in Eq. (4) and Table 1.

Table 1
Gaussian parametrisation of the inter-wafer gaps.

	Position (mm)	σ (mm)	a
x direction	−30.0	4.3	0.143
y direction	−8.4	3.2	0.198

Table 2
Gaussian parametrisations of the inter-wafer gaps for different electron energies, for data and simulation.

Energy (GeV)	σ_x (mm) Data/MC	a_x (%) Data/MC	σ_y (mm) Data/MC	a_y (%) Data/MC
6	4.6/4.5	15/16	3.1/3.3	20/21
10	4.2/4.3	15/17	3.1/3.2	20/23
15	4.2/4.3	15/17	3.2/3.1	20/24
20	4.5/4.3	15/18	3.2/3.1	20/25
30	4.6/4.3	15/18	3.3/3.0	20/27

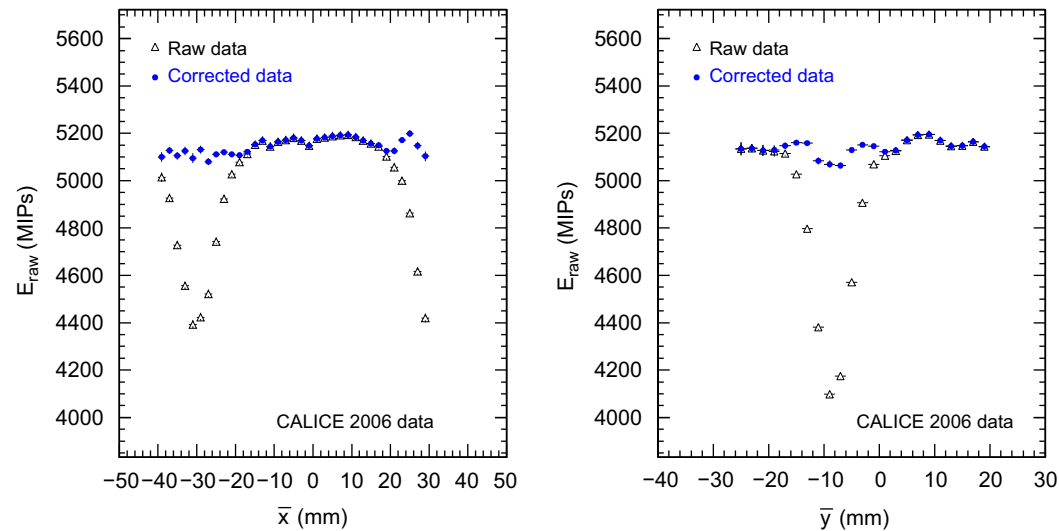


Fig. 9. Mean E_{raw} as a function of the shower barycentre coordinates for 20 GeV electrons, before (open triangles) and after the inter-wafer gap corrections (solid circles) were applied to E_{raw} .

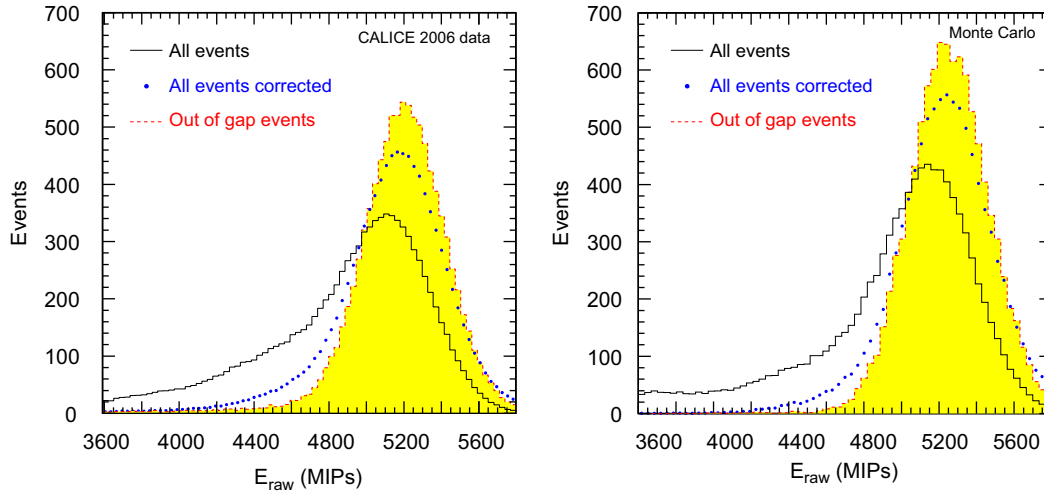


Fig. 10. Energy distributions for 20 GeV electrons, for data (left) and simulation (right). The distributions are shown for events outside the inter-wafer gaps (shaded histogram), all events without inter-wafer gap corrections (open histogram) and all events with inter-wafer gap corrections (solid circles). The histograms are normalised to the same number of entries.

Table 3

Summary of the electron events selected for this analysis.

Energy (GeV)	Date (2006)	Beam momentum spread (%)	Fraction of selected triggers (%)	Data statistics (keVts)	Monte Carlo statistics (keVts)
6	October	1.11	6.2	6.6	20.2
10	August, October	0.22–0.73	8.5	43.1	54.0
12	October	0.22–0.44	9.6	27.2	26.7
15	August, October	0.26–0.73	9.1	51.4	50.5
20	August	0.22–0.73	11	62.9	44.8
30	August	0.22	16.5	42.3	52.8
40	August	0.24	13.2	22.9	55.7
45	August	0.22–0.24	12	108.6	98.3

In the case of data sets with different nominal momentum-spreads of the beam for the same mean energy only the variation range is indicated. The numbers of simulated electron events for each energy, available after the selections, are also shown.

centre, the shower barycentre for selected events is required to be at a distance larger than 17.2 mm from the centre of the inter-wafer gap along x and 12.76 mm away from the centre of the y gap. These selections retain about 20% of the electrons.

A sustained R&D effort is being made to reduce the non-active areas, both by reducing the size of the inter-wafer gaps and by increasing the size of the wafers. The next ECAL prototype will have 16×16 Si pads in a wafer of size 9×9 cm² which leads to a significant decrease of the non-active areas.

A summary of the selected electron and positron data is shown in Table 3. The number of simulated events available for each energy is also indicated.

6. Performance studies

6.1. ECAL sampling fraction scheme

The ECAL is made of 30 layers grouped in three modules of 10 layers each [3]. Each tungsten sheet has the same thickness in a given module. However, as can be derived from Fig. 11, where one passive tungsten layer sandwiched between two active silicon layers is shown, two successive silicon layers are either separated by one thickness of tungsten or by the same thickness of tungsten plus two thicknesses of PCB, aluminum and carbon-fibre-epoxy composite. A different sampling fraction, defined as the ratio of the energy deposited in the active medium to the total energy deposit (sum of the energy deposits in the active and passive

medium), is therefore expected for the even and the odd layers of the same calorimeter module.

The easiest method to investigate this difference is to compare in each module the mean energy deposits in odd and even layers. For the first module, if the shower profile is neglected, the ratio of the two is

$$R = \frac{E_{\text{odd}}}{E_{\text{even}}} = 1 + \eta \quad (5)$$

with η being, approximately, the ratio of the non-tungsten radiation length to the tungsten radiation length.

When counting the layers starting from zero, the odd layers are systematically shifted compared to the even layers towards the shower maximum and the measurement of R is biased by the shower development. To overcome this bias, R is measured twice, either comparing the odd layers with the average of the surrounding even layers, or comparing the even layers with the average of the neighbouring odd layers

$$R' = \frac{\langle E_1 + E_3 + E_5 + E_7 \rangle}{\left\langle \frac{E_0 + E_2}{2} + \frac{E_2 + E_4}{2} + \frac{E_4 + E_6}{2} + \frac{E_6 + E_8}{2} \right\rangle} \quad (6)$$

$$R'' = \frac{\left\langle \frac{E_1 + E_3}{2} + \frac{E_3 + E_5}{2} + \frac{E_5 + E_7}{2} + \frac{E_7 + E_9}{2} \right\rangle}{\langle E_2 + E_4 + E_6 + E_8 \rangle} \quad (7)$$

where E_n is the energy deposit in the layer number n and the brackets indicate that mean values are used. The value of η is taken as the average of $R' - 1$ and $R'' - 1$, while the difference

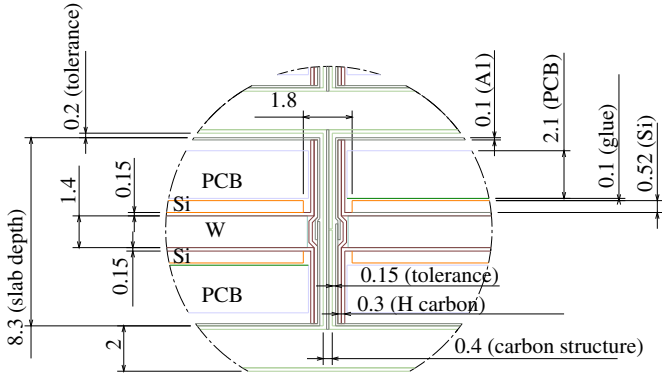


Fig. 11. Details of one ECAL slab, showing one passive tungsten layer sandwiched between two active silicon layers. The dimensions are in mm. In contrast to the upper silicon layer which is preceded by a layer of tungsten only, the lower silicon layer is preceded by a larger passive layer: the PCB, aluminum, glue and carbon structure as well as the tungsten.

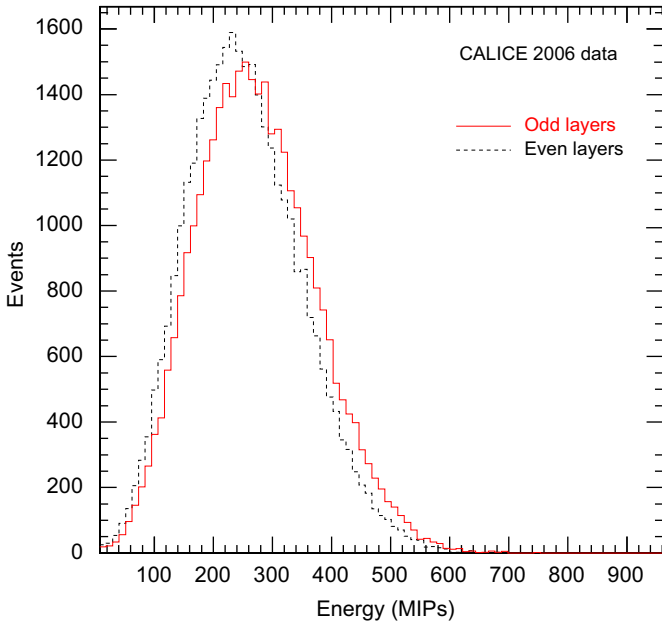


Fig. 12. Energy deposits in odd layers (continuous histogram) and in their surrounding even layers (dashes) for 20 GeV electrons, in the first ECAL module.

between them gives a conservative estimate of the systematic uncertainty due to the shower shape. As an example, the distributions of the energy deposits in the odd and even layers are shown in Fig. 12 for 20 GeV electrons.

In computing the total response of the calorimeter, the sampling fraction for layer i is given by $w_i = K$ for even layers and $w_i = K + \eta$ for the odd layers, with $K = 1, 2, 3$ in modules 1, 2, 3, respectively.

The values of η , obtained using the first module and for different beam energies, are displayed in Fig. 13. The overall value is $(7.2 \pm 0.2 \pm 1.7)\%$. The measurement of η using the second and third module gives compatible results and the corresponding value obtained from simulation is $(4.7 \pm 0.2 \pm 2.0)\%$.

6.2. Linearity and energy resolution

The total response of the calorimeter is calculated as

$$E_{\text{rec}}(\text{MIPs}) = \sum_i w_i E_i \quad (8)$$

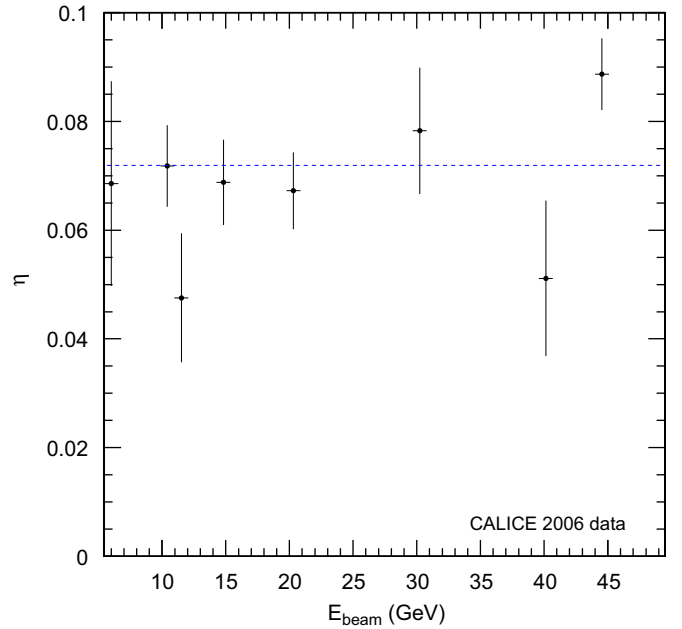


Fig. 13. Values of η (see Eq. (5)) as a function of the beam energy. The uncertainties are statistical and the dashed line gives the average value of η .

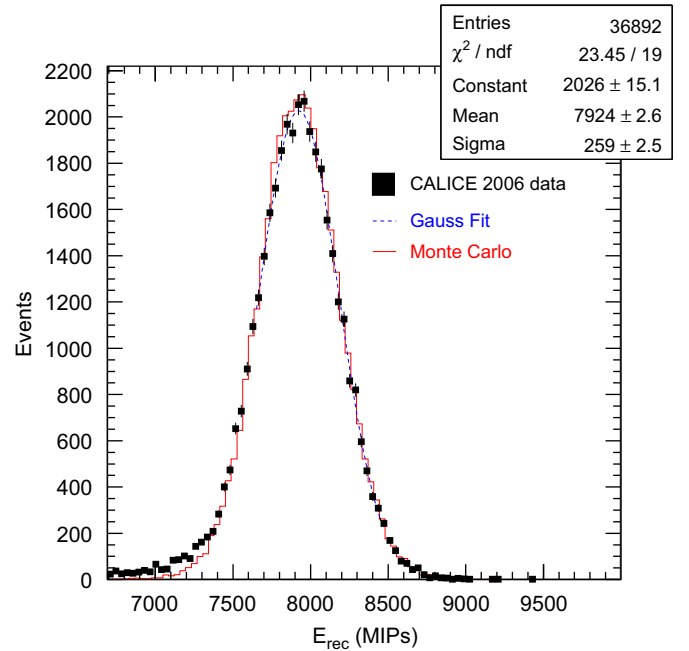


Fig. 14. Gaussian parametrisation of E_{rec} for 30 GeV electron data (dashes). The range of the fit is $[-\sigma, +2\sigma]$. The data (solid squares) and simulation (continuous line) are superimposed.

with w_i the sampling fraction for the layer i . Its distribution for electrons at 30 GeV is shown in Fig. 14, together with a fit using a Gaussian function in the range $[-\sigma, +2\sigma]$. There is reasonably good agreement between data and simulation. An asymmetric range is chosen for the fit in order to reduce sensitivity to pion background, to radiative effects upstream of the calorimeter, and to any residual influence of the inter-wafer gaps. The position of the peak is the mean energy response (called in the following E_{mean}) and its distribution is shown in Fig. 15 as a function of the beam energy. The uncertainties on E_{mean} are those estimated from the fit.

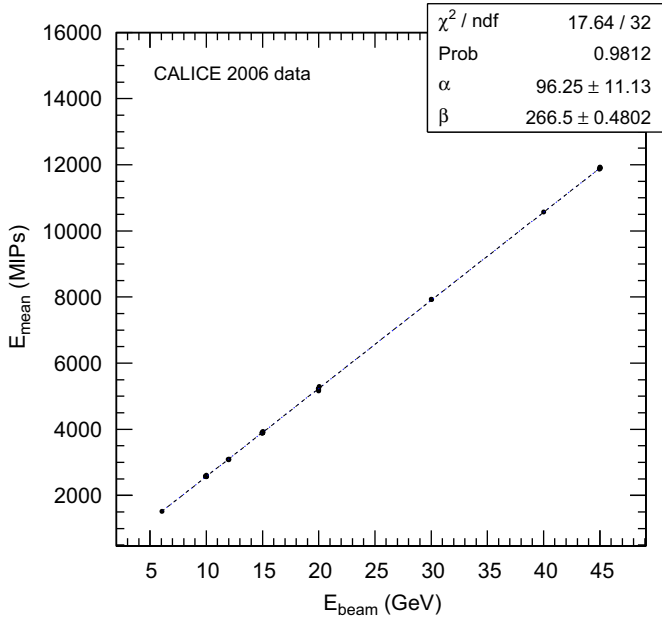


Fig. 15. Energy response of the ECAL as a function of the beam energy. For clarity, all the runs around the same nominal energy of the beam were combined in one entry for the plot, for which entry the uncertainty was estimated assuming that the uncertainties on the individual runs were uncorrelated.

From the dispersion of E_{mean} in the different runs at the same nominal beam energy, the uncertainty on the mean energy of the beam, E_{beam} , was estimated to be

$$\frac{\Delta E_{\text{beam}}}{E_{\text{beam}}} = \frac{0.12}{E_{\text{beam}}(\text{GeV})} \oplus 0.1\%. \quad (9)$$

The first term is related to hysteresis in the bending magnets, while the calibration and the uncertainties on the collimator geometry give the constant term. For comparison, in Ref. [9], this uncertainty, was quoted as

$$\frac{\Delta E_{\text{beam}}}{E_{\text{beam}}} = \frac{0.25}{E_{\text{beam}}(\text{GeV})} \oplus 0.5\%. \quad (10)$$

The first of these parametrisations of the uncertainty (Eq. (9), reflecting run-to-run variations in the mean energy of the beam) is used in the following, except for checks of systematic uncertainties.

The mean energy response can be parametrised as $E_{\text{mean}} = \beta \cdot E_{\text{beam}} - \alpha$, while the *measured* energy E_{meas} is given by $E_{\text{meas}} = E_{\text{mean}} + \alpha$. The parameter β is a global MIP to GeV calibration factor. The offset α is partly due to the rejection of the low energy hits and it increases steadily with the hit energy threshold, as displayed in Fig. 16. In the same figure the values of the offset, as expected from simulation, are also shown. The systematic uncertainty affecting the offset measurement is estimated to be 8.7 MIPs, as follows. An upper estimate for the systematic uncertainty due to the incomplete knowledge of the beam line more than 60 m upstream of the ECAL is obtained by not applying any T_{max} selection (see Section 5.3) on the data. Another systematic uncertainty taken into account is induced by the fitting range for E_{mean} and the minimal accepted distance between the shower barycentre and the nearest inter-wafer gap. They are of 5.6 and 5 MIPs, respectively, and dominate all the other uncertainties considered. The disagreement between the data offset and the offset expected from simulation is somewhat greater than the estimated systematic uncertainties. It could however be accounted for by an overall uncertainty on the

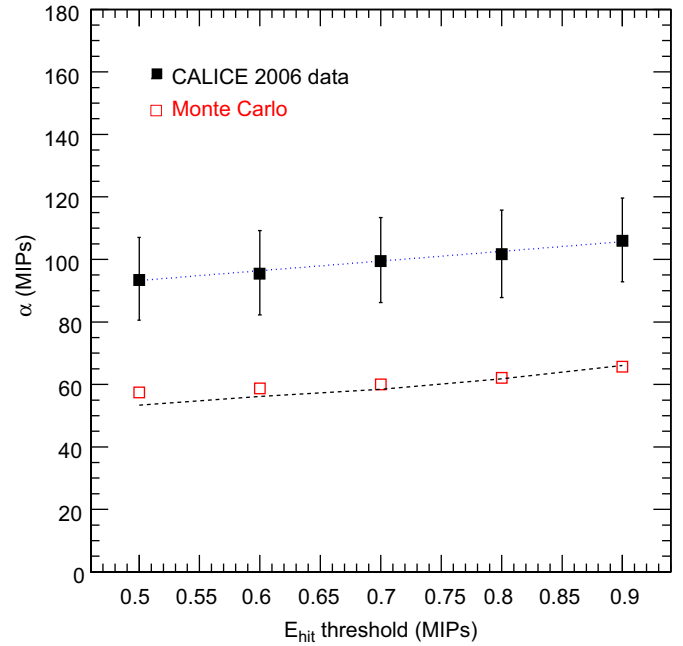


Fig. 16. Variation of the linearity offset with the hit energy threshold: data (solid squares) and simulation (open squares). The uncertainties for the data points are both statistical and systematic. The dashed line shows the effect on the data offset assuming a systematic shift of -150 MeV in the beam energy scale.

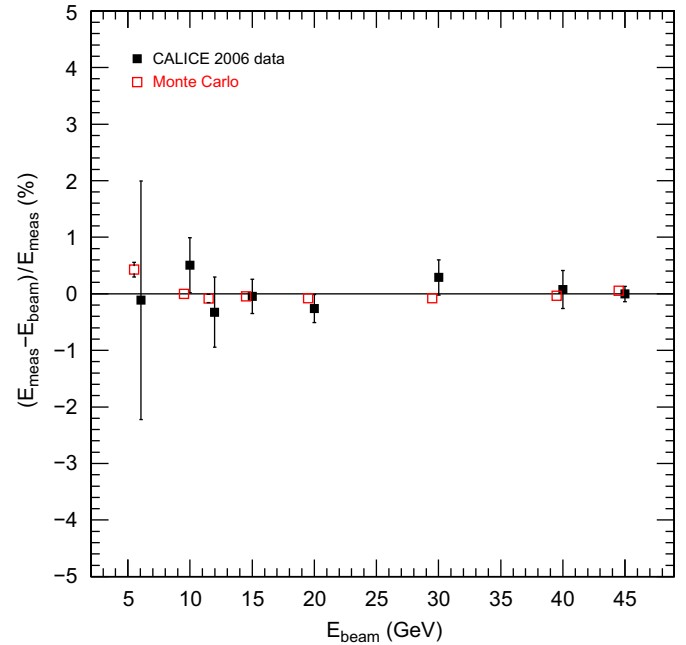


Fig. 17. The linearity of the response, $(E_{\text{meas}} - E_{\text{beam}})/E_{\text{meas}}$, as a function of the beam energy, for data (solid squares) and simulation (open squares). All the runs around the same nominal energy of the beam were combined in one entry, for which the uncertainty was estimated assuming that the uncertainties on the individual runs were uncorrelated. For clarity, the Monte Carlo points were artificially shifted along the x axis around the nominal E_{beam} .

absolute energy scale of the beam of 150 MeV, which would not have been revealed by the tests leading to Eq. (9).

The linearity of the response, $(E_{\text{meas}} - E_{\text{beam}})/E_{\text{meas}}$ (with E_{meas} converted from MIPs to GeV using a constant 266 MIPs/GeV conversion factor, as obtained from Fig. 15), is shown in Fig. 17 as a function of the beam energy. The residuals are within

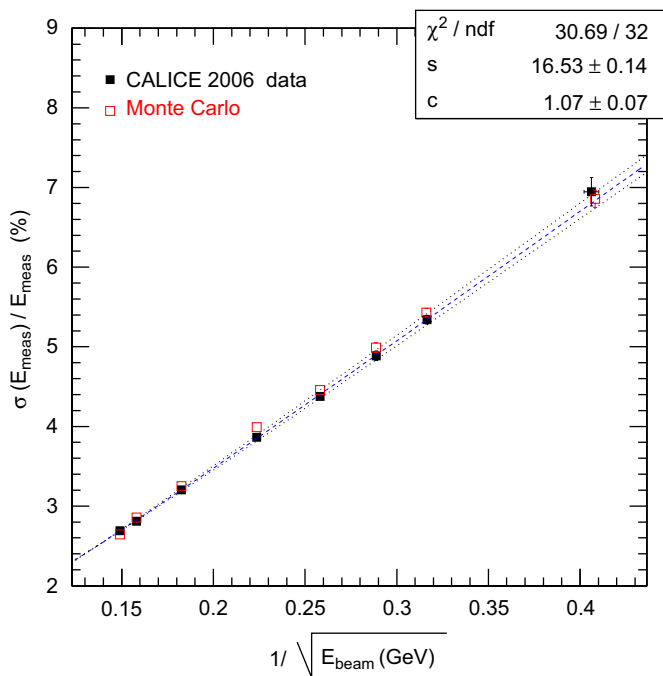


Fig. 18. Relative energy resolution ($\sigma(E_{\text{meas}})/E_{\text{meas}}$) as a function of $1/\sqrt{E_{\text{beam}}}$ (solid squares), and its usual parametrisation as $s/\sqrt{E} \oplus c$. For clarity, the 35 runs available were combined into eight different beam energy points for the plot. For the parametrisation of the energy resolution each run was however treated individually. The values expected from simulation are shown (open squares). The dashed line gives the fitted resolution for data (Eq. (11)), and the dotted lines correspond to its variation when the beam energy scale is shifted by ± 300 MeV.

approximately the 1% level and are consistent with zero non-linearity. Data and simulation agree within one standard deviation.

The relative energy resolution, $\sigma(E_{\text{meas}})/E_{\text{meas}}$, as shown in Fig. 18, can be parametrised by a quadrature sum of stochastic and constant terms

$$\frac{\sigma(E_{\text{meas}})}{E_{\text{meas}}} = \left(\frac{16.53 \pm 0.14(\text{stat}) \pm 0.4(\text{syst})}{\sqrt{E}(\text{GeV})} \oplus (1.07 \pm 0.07(\text{stat}) \pm 0.1(\text{syst})) \right) \% \quad (11)$$

where the intrinsic momentum spread of the beam was subtracted from the ECAL data [6]. The contribution of a possible $1/E$ term in the energy resolution is negligible. As in the case of the offset, the dominant systematic uncertainty is due to the cut on T_{max} (0.3% in the case of the stochastic term). A systematic shift in the beam energy scale of 150 MeV would lead to an additional variation of 0.13% in the stochastic term. The expected resolution from simulation agrees with the measured resolution of the prototype to within $\sim 2\%$ of its value at all energies, except at 20 GeV where the discrepancy is $\sim 3\%$. The Monte Carlo resolution can be parametrised by

$$\left[\frac{\sigma(E_{\text{meas}})}{E_{\text{meas}}} \right]^{\text{MC}} = \left(\frac{17.06 \pm 0.13}{\sqrt{E}(\text{GeV})} \oplus (0.82 \pm 0.09) \right) \%. \quad (12)$$

Examples of the systematic studies of the linearity and resolution parameters are shown in Tables 4–6. The dependence of the parameters on the minimal accepted distance between the shower barycentre and the nearest inter-wafer gap is shown in Table 4. In this study, the energy threshold for considering the hits is 0.6 MIPs. In addition, the effect of varying this threshold is presented in Table 5. In order to investigate the potential effects linked to the beam position, the energy response is also compared

Table 4

Impact of the distance of the shower to the inter-wafer gaps on the ECAL linearity and resolution.

	Shower distance to the gaps (in standard deviations)			
	3.5	4	4.5	5
χ^2/ndf (linearity)	16.8/32	17.6/32	18.9/32	24.2/32
α (MIPs)	93.9 ± 11.1	96.3 ± 11.2	97.8 ± 11.5	99.1 ± 11.6
β (MIPs/GeV)	266.3 ± 0.5	266.6 ± 0.5	266.8 ± 0.5	266.8 ± 0.5
Stochastic term of energy resolution (%)	16.7 ± 0.1	16.6 ± 0.1	16.4 ± 0.2	16.3 ± 0.2
Constant term of energy resolution (%)	1.0 ± 0.1	1.0 ± 0.1	1.1 ± 0.1	1.2 ± 0.1

The distance is given in terms of standard deviations to the gap centre, with the standard deviation defined by the Gaussian parametrisation of the gaps.

Table 5

Impact of the threshold imposed for the hit energy on the ECAL linearity and resolution.

	E_{hit} threshold (MIPs)		
	0.5	0.7	0.9
χ^2/ndf (linearity)	18.0/32	17.8/32	18.0/32
α (MIPs)	93.0 ± 11.2	98.9 ± 11.1	105.6 ± 11.1
β (MIPs/GeV)	266.8 ± 0.5	266.3 ± 0.5	265.8 ± 0.5
Stochastic term of energy resolution (%)	16.6 ± 0.1	16.5 ± 0.1	16.6 ± 0.1
Constant term of energy resolution (%)	1.0 ± 0.1	1.1 ± 0.1	1.1 ± 0.1

Table 6

Response to electrons crossing the right-hand side and the upper part of the ECAL.

	Right-hand side	Upper part
α (MIPs)	96.1 ± 10.9	97.7 ± 11
β (MIPs/GeV)	266.6 ± 0.5	266.8 ± 0.5
Stochastic term of energy resolution (%)	16.8 ± 0.1	16.8 ± 0.2
Constant term of energy resolution (%)	1.1 ± 0.1	1.1 ± 0.1

for showers with barycentres located in the right-hand side (negative x coordinates) and in the upper half of the detector (upper row of wafers), as summarised in Table 6. The results of all checks are consistent. Since data were taken in both August and October 2006, it was also possible to check the response stability in time and no significant differences between the two data samples are observed.

7. Conclusion

The response to normally incident electrons of the CALICE Si-W electromagnetic calorimeter was measured for energies between 6 and 45 GeV, using the data recorded in 2006 at CERN.

The calorimeter response is linear to within approximately 1%. The energy resolution has a stochastic term of $(16.53 \pm 0.14(\text{stat}) \pm 0.4(\text{syst}))\%/\sqrt{E}(\text{GeV})$, whereas the constant term is $(1.07 \pm 0.07(\text{stat}) \pm 0.1(\text{syst}))\%$.

The material far upstream in the beam line leads to significant differences between some of the measured distributions and the expectations from simulation. However, they do not have a large impact on the main results, i.e. ECAL linearity and energy resolution, for which better than 5% agreement between data and simulation is achieved.

Acknowledgements

We would like to thank the technicians and the engineers who contributed to the design and construction of the prototypes, including U. Cornett, G. Falley, K. Gadow, P. Göttlicher, S. Karstensen and P. Smirnov. We also gratefully acknowledge the DESY and CERN managements for their support and hospitality, and their accelerator staff for the reliable and efficient beam operation. We would like to thank the HEP group of the University of Tsukuba for the loan of drift chambers for the DESY test-beam. The authors would like to thank the RIMST (Zelenograd) group for their help and sensors manufacturing. This work was supported by the Bundesministerium für Bildung und Forschung, Germany; by the DFG cluster of excellence “Origin and Structure of the Universe”; by the Helmholtz-Nachwuchsgruppen Grant VH-NG-206; by the BMBF, Grant numbers 05HS6VH1 and 05HS6GU1; by the Alexander von Humboldt Foundation (Research Award IV, RUS1066839 GSA); by joint Helmholtz Foundation and RFBR Grant HRJRG-002, Russian Agency for Atomic Energy, ISTC Grant 3090;

by Russian Grants SS-1329.2008.2 and RFBR0402/17307a and by the Russian Ministry of Education and Science; by CRI(MST) of MOST/KOSEF in Korea; by the US Department of Energy and the US National Science Foundation; by the Ministry of Education, Youth and Sports of the Czech Republic under the Projects AV0 Z3407391, AV0 Z10100502, LC527 and by the Grant Agency of the Czech Republic under the Project 202/05/0653; and by the Science and Technology Facilities Council, UK.

References

- [1] T. Behnke, et al. (Eds.), Reference Design Report Volume 4: Detectors. Available at <http://lcdev.kek.jp/RDR>.
- [2] D. Buskulic, et al., Nucl. Instr. and Meth. A 360 (1995) 481; J.-C. Brient, Improving the jet reconstruction with the particle flow method: an introduction, in: Proceedings of 11th International Conference on Calorimetry in High-Energy Physics (Calor 2004), Perugia, Italy, March 2004.
- [3] M. Anduze, et al., J. Instr. 3 (2008) P08001 33pp.
- [4] F. Sefkow, The scintillator HCAL testbeam prototype, in: Proceedings of 2005 International Linear Collider Workshop (LCWS 2005), Stanford, California, March 2005.
- [5] D. Chakraborty, The tail-catcher/muon tracker for the CALICE test beam, in: Proceedings of 2005 International Linear Collider Workshop (LCWS 2005), Stanford, California, March 2005.
- [6] Description of the CERN H6 testbeam area. Available at <http://ab-div-atb-ea.web.cern.ch/ab-div-atb-ea/BeamsAndAreas/>.
- [7] Mokka Geant4 application for linear collider detectors, see <http://polzope.in2p3.fr:8081/MOKKA>.
- [8] S. Agostinelli, et al., Nucl. Instr. and Meth. A 506 (2003) 250.
- [9] S. Akhmadaliev, et al., Nucl. Instr. and Meth. A 449 (2000) 461; M. Aharrouche, et al., Nucl. Instr. and Meth. A 568 (2006) 601.